

# Optical properties of ordered carbon nanotube arrays grown in porous anodic alumina templates

John Zuidema,<sup>1</sup> Xiulin Ruan,<sup>1,\*</sup> and Timothy S. Fisher<sup>1,2</sup>

<sup>1</sup>*School of Mechanical Engineering and Birck Nanotechnology Center, Purdue University, West Lafayette, Indiana 47907, USA*

<sup>2</sup>*tsfisher@purdue.edu*  
*ruan@purdue.edu*

**Abstract:** We have synthesized ordered carbon nanotube (CNT) arrays in porous anodic alumina (PAA) matrix, and have characterized their total optical reflectance and bi-directional reflectance distribution function after each processing step of the microwave plasma chemical vapor deposition process (MPCVD). For a PAA sample without CNT growth, the reflectance shows an oscillating pattern with wavelength that agrees reasonably with a multilayer model. During the MPCVD process, heating the sample significantly reduces the reflectance by 30-40%, the plasma treatment reduces the reflectance by another 5-10%, and the CNT growth further reduces the reflectance by 2-3%. After an atomic layer deposition (ALD) process, the reflectance increases to the embedded CNT arrays. After etching and exposure of CNT tips, the reflectance almost returns to the original pattern with slightly higher reflectance. Bi-directional reflectance distribution function (BRDF) measurements show that the CNT-PAA surface is quite specular as indicated by a large lobe at the specular angle, while the secondary lobe can be attributed to surface roughness.

©2013 Optical Society of America

**OCIS codes:** (310.1860) Deposition and fabrication; (310.6628) Subwavelength structures, nanostructures; (310.6860) Thin films, optical properties.

---

## References and links

1. S. Iijima, "Helical microtubules of graphitic carbon," *Nature* **354**(6348), 56–58 (1991).
2. K. Kempa, B. Kimball, J. Rybczynski, Z. P. Huang, P. F. Wu, D. Steeves, M. Sennett, M. Giersig, D. V. G. L. N. Rao, D. L. Carnahan, D. Z. Wang, J. Y. Lao, W. Z. Li, and Z. F. Ren, "Photonic crystals based on periodic arrays of aligned carbon nanotubes," *Nano Lett.* **3**(1), 13–18 (2003).
3. E. Lidorikis and A. C. Ferrari, "Photonics with multiwall carbon nanotube arrays," *ACS Nano* **3**(5), 1238–1248 (2009).
4. K. Kempa, J. Rybczynski, Z. P. Huang, K. Gregorczyk, A. Vidan, B. Kimball, J. Carlson, G. Benham, Y. Wang, A. Herczynski, and Z. F. Ren, "Carbon nanotubes as optical antennae," *Adv. Mater.* **19**(3), 421–426 (2007).
5. X. J. Wang, J. D. Flicker, B. J. Lee, W. J. Ready, and Z. M. Zhang, "Visible and near-infrared radiative properties of vertically aligned multi-walled carbon nanotubes," *Nanotechnology* **20**(21), 215704 (2009).
6. S. Shoji, H. Suzuki, R. P. Zaccaria, Z. Sekkat, and S. Kawata, "Optical polarizer made of uniaxially aligned short single-wall carbon nanotubes embedded in a polymer film," *Phys. Rev. B* **77**(15), 153407 (2008).
7. Z. P. Yang, L. J. Ci, J. A. Bur, S. Y. Lin, and P. M. Ajayan, "Experimental observation of an extremely dark material made by a low-density nanotube array," *Nano Lett.* **8**(2), 446–451 (2008).
8. H. Bao, X. L. Ruan, and T. S. Fisher, "Optical properties of ordered vertical arrays of multi-walled carbon nanotubes from FDTD simulations," *Opt. Express* **18**(6), 6347–6359 (2010).
9. F. Keller, M. S. Hunter, and D. L. Robinson, "Structural features of oxide coatings on aluminium," *J. Electrochem. Soc.* **100**(9), 411–419 (1953).
10. M. R. Maschmann, A. D. Franklin, A. Scott, D. B. Janes, T. D. Sands, and T. S. Fisher, "Lithography-free in situ Pd contacts to templated single-walled carbon nanotubes," *Nano Lett.* **6**(12), 2712–2717 (2006).
11. A. D. Franklin, D. B. Janes, J. C. Claussen, T. S. Fisher, and T. D. Sands, "Independently addressable fields of porous anodic alumina embedded in SiO<sub>2</sub> on Si," *Appl. Phys. Lett.* **92**(1), 013122 (2008).

12. J. D. Edwards and T. Keller, "The structure of anodic oxide coatings," *Transactions of the American Institute of Mining and Metallurgical Engineers* **156**, 288–299 (1944).
13. H. Masuda, F. Hasegawa, and S. Ono, "Self-ordering of cell arrangement of anodic porous alumina formed in sulfuric acid solution," *J. Electrochem. Soc.* **144**(5), L127–L130 (1997).
14. H. Masuda, H. Yamada, M. Satoh, H. Asoh, M. Nakao, and T. Tamamura, "Highly ordered nanochannel-array architecture in anodic alumina," *Appl. Phys. Lett.* **71**(19), 2770–2772 (1997).
15. O. Jessensky, F. Muller, and U. Gosele, "Self-organized formation of hexagonal pore arrays in anodic alumina," *Appl. Phys. Lett.* **72**(10), 1173–1175 (1998).
16. Z. J. Sun and H. K. Kim, "Growth of ordered, single-domain, alumina nanopore arrays with holographically patterned aluminum films," *Appl. Phys. Lett.* **81**(18), 3458–3460 (2002).
17. H. Asoh, K. Nishio, M. Nakao, A. Yokoo, T. Tamamura, and H. Masuda, "Fabrication of ideally ordered anodic porous alumina with 63 nm hole periodicity using sulfuric acid," *J. Vac. Sci. Technol. B* **19**(2), 569–572 (2001).
18. A. P. Li, F. Muller, A. Birner, K. Nielsch, and U. Gosele, "Hexagonal pore arrays with a 50–420 nm interpore distance formed by self-organization in anodic alumina," *J. Appl. Phys.* **84**(11), 6023–6026 (1998).
19. E. C. Walter, K. Ng, M. P. Zach, R. M. Penner, and F. Favier, "Electronic devices from electrodeposited metal nanowires," *Microelectron. Eng.* **61–62**, 555–561 (2002).
20. S. H. Jeong, H. Y. Hwang, S. K. Hwang, and K. H. Lee, "Carbon nanotubes based on anodic aluminum oxide nano-template," *Carbon* **42**(10), 2073–2080 (2004).
21. H. Y. Jung, J. Kim, J. Hahn, and J. S. Suh, "Well-ordered semiconducting linearly joined carbon nanotube devices at room temperature," *Chem. Phys. Lett.* **402**(4-6), 535–538 (2005).
22. P. L. Chen, J. K. Chang, C. T. Kuo, and F. M. Pan, "Anodic aluminum oxide template assisted growth of vertically aligned carbon nanotube arrays by ECR-CVD," *Diamond Related Materials* **13**(11-12), 1949–1953 (2004).
23. M. J. Kim, T. Y. Lee, J. H. Choi, J. B. Park, J. S. Lee, S. K. Kim, J. B. Yoo, and C. Y. Park, "Growth of carbon nanotubes with anodic aluminum oxide formed on the catalytic metal-coated Si substrate," *Diamond Related Materials* **12**(3-7), 870–873 (2003).
24. J. S. Lee and J. S. Suh, "Uniform field emission from aligned carbon nanotubes prepared by CO disproportionation," *J. Appl. Phys.* **92**(12), 7519–7522 (2002).
25. J. H. Yen, I. C. Leu, M. T. Wu, C. C. Lin, and M. H. Hon, "Density control for carbon nanotube arrays synthesized by ICP-CVD using AAO/Si as a nanotemplate," *Electrochem. Solid-State Lett.* **7**(8), H29–H31 (2004).
26. M. R. Maschmann, A. D. Franklin, T. D. Sands, and T. S. Fisher, "Optimization of carbon nanotube synthesis from porous anodic Al-Fe-Al templates," *Carbon* **45**(11), 2290–2296 (2007).
27. S. Hofmann, G. Csányi, A. C. Ferrari, M. C. Payne, and J. Robertson, "Surface diffusion: The low activation energy path for nanotube growth," *Phys. Rev. Lett.* **95**(3), 036101 (2005).
28. M. R. Maschmann, A. D. Franklin, P. B. Amama, D. N. Zakharov, E. A. Stach, T. D. Sands, and T. S. Fisher, "Vertical single- and double-walled carbon nanotubes grown from modified porous anodic alumina templates," *Nanotechnology* **17**(15), 3925–3929 (2006).
29. G. F. Zhong, T. Iwasaki, K. Honda, Y. Furukawa, I. Ohdomari, and H. Kawarada, "Very high yield growth of vertically aligned single-walled carbon nanotubes by point-arc microwave plasma CVD," *Chemical Vapor Deposition* **11**(3), 127–130 (2005).
30. S. Fournier-Bidoz, V. Kitaev, D. Routkevitch, I. Manners, and G. A. Ozin, "Highly ordered nanosphere imprinted nanochannel alumina (NINA)," *Adv. Mater.* **16**(23-24), 2193–2196 (2004).
31. E. F. Schubert, "Refractive index and extinction coefficient of materials," (2004), <http://homepages.rpi.edu/~schubert/Educational-resources/Materials-Refractive-index-and-extinction-coefficient.pdf>.
32. J. A. Kong, *Electromagnetic Wave Theory* (Wiley, 1990).
33. K. E. Torrance and E. M. Sparrow, "Theory for Off-Specular Reflection from Roughened Surfaces," *J. Opt. Soc. Am.* **57**(9), 1105–1114 (1967).
34. A. D. Franklin, R. A. Sayer, T. D. Sands, D. B. Janes, and T. S. Fisher, "Vertical Carbon Nanotube Devices With Nanoscale Lengths Controlled Without Lithography," *IEEE Trans. NanoTechnol.* **8**(4), 469–476 (2009).
35. D. Bergström, J. Powell, and A. F. H. Kaplan, "A ray-tracing analysis of the absorption of light by smooth and rough metal surfaces," *J. Appl. Phys.* **101**(11), 113504 (2007).
36. A. H. Wang, P. F. Hsu, and J. J. Cai, "Modeling bidirectional reflection distribution function of microscale random rough surfaces," *Journal of Central South University of Technology* **17**(2), 228–234 (2010).

## 1. Introduction

In 1991, Iijima first grew carbon nanotubes using an arc-discharge method [1]. Carbon nanotubes (CNTs) are composed of individual sheets of graphene, rolled up into cylinders that can be only a few nanometers thick. CNTs are categorized into two different types: single walled carbon nanotubes (SWCNTs), composed of one graphene sheet, and multi-walled carbon nanotubes (MWCNTs), composed of several sheets wrapped around each other in concentric rings.

CNTs can be grown in arrays for promising optical, electrical, and thermal applications. In general, optical properties of CNT arrays depend on both the dielectric function of each individual CNT and the long-range configuration of the array. To date, many interesting optical properties have been observed in CNT arrays grown without a template, such as photonic crystal effects [2, 3], directional emission [4, 5], wavelength-selective emission and polarization-dependent reflection [6], and high absorptivity [7, 8].

On the other hand, CNT arrays can also be grown in templates, among which porous anodic alumina (PAA) has been well-studied [9]. The configuration of CNT arrays grown in PAA holds promise for electronic devices based on carbon nanotubes [10, 11]. PAA is an arrangement of semi-ordered pores that are the result of anodization on an Al film, and the pores protect CNTs grown in the microwave plasma chemical vapor deposition (MPCVD) system. The presence of CNTs can possibly modify the optical properties of the PAA or exhibit optical antenna effect. Such knowledge is also useful for using CNT arrays as additives to tune the optical properties of the matrix material. However, no measurements or analysis of optical properties have been performed on template-grown CNT arrays so far.

In this work, we have synthesized CNT arrays in PAA templates and measured their optical properties. Well-ordered and high-yield CNT growth in porous anodic alumina (PAA) templates was established by varying conditions such as electrical bias and plasma treatments. Controlled variation of process (ALD, etching) has been achieved. Optical reflectance has been characterized on CNT arrays samples, and tunable thermal radiative properties in total reflectance and spectra have been observed.

## 2. Growth and preparation of CNT arrays

Some of the earliest studies of nanoscale templating involved porous anodic alumina (PAA) [9, 12]. PAA is formed by anodic oxidation of Al in an acidic electrolyte. The Al is typically either a foil that is several tens of microns thick or a substrate-supported thin film. The resulting alumina template consists of vertical pores in a naturally occurring hexagonal arrangement [13–17]. The pore diameter is linearly dependent on the anodization electrolyte and voltage—demonstrated pore diameters range from sub-10 nm to several hundred nanometers [18, 19]. Today PAA is used in myriad applications, from a dye-support on the casing of commercial aluminum products (*e.g.*, flashlights, lipstick cases) to a template for supporting the electrochemical formation of nanowires [18].

The earliest reports of CNTs templated in PAA involve MWCNTs synthesized with or without deposited catalyst in the pores. When synthesizing MWCNTs in PAA without a catalyst, the main formation mechanism is the adsorption of carbon on the alumina pore walls by the decomposition of hydrocarbons, and this process yields tubes of low crystalline quality [20, 21]. Reported MWCNT synthesis methods utilizing a catalyst include the use of Co [22–24] or Ni [23–25] deposited within the pores followed by MWCNT synthesis. These processes yield MWCNTs that take on the diameter of the pores and typically have a high concentration of disordered carbon, but they provide excellent control of the length and diameter of the MWCNTs by varying the dimensions of the PAA.

However, SWCNT synthesis from customized templates or catalysts is more difficult because of their relatively high activation energy in comparison to MWCNTs [26, 27]. Additionally, nucleation of SWCNTs requires catalyst particles of diameters less than a few nanometers, a size that is not easily achieved when fashioning a catalyst within a template. These two obstacles of high activation energy and difficult catalyst particle size-control are overcome in the present work by burying a Fe catalyst layer in a PAA template and synthesizing in a high-temperature microwave plasma chemical vapor deposition (MPCVD) environment [28]. The plasma helps to lower the required thermal activation energy by providing a separate means for dissociating the hydrocarbon precursors, thus relieving part of the energy burden from the catalyst particle. Secondly, covering Fe with a thin layer (few nanometers) of alumina (as is the case on the pore sidewalls of the modified PAA template)

raises the surface diffusion barrier of the catalytic Fe particles and thus mitigates agglomeration [29].

The catalytically active PAA template is formed by first depositing a 100 nm Ti/100 nm Al/1 nm Fe/1000 nm Al film stack on a SiO<sub>2</sub> covered Si wafer, as shown in Fig. 1(a). The Ti serves as an adhesion layer for the film and a conductive layer for anodization and other post-processing. Typically, the first (bottom) Al layer is 100 – 200 nm thick, while the top Al is 200 – 1000 nm thick, and the sandwiched Fe layer is approximately 1 nm thick. Anodization is carried out in an acidic electrolyte maintained at 5°C under a constant voltage that is applied with respect to a Pt gauze counter electrode. While several electrolytes can be used in the formation of PAA, 0.3M oxalic acid provides pores of ≈20 nm diameter at an anodization voltage of 40 V, which is a good average size when working with the present catalytically active PAA. Larger pores or smaller pores can be obtained by anodizing in phosphoric acid or sulfuric acid, respectively [30].

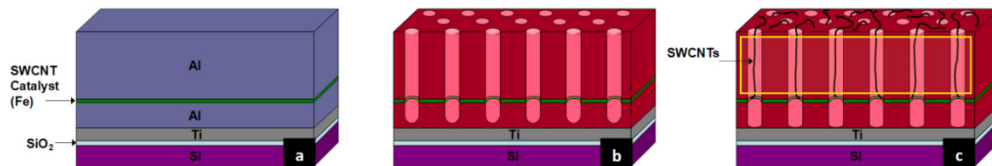


Fig. 1. Cross-sectional schematic of: (a) metal film stack deposited on Si wafer, (b) PAA film after anodization, and (c) SWCNTs emerging from PAA pores after undergoing MPCVD synthesis; the box highlights the vertical SWCNT channels.

Anodization of Al occurs by the exchange of Al<sup>3+</sup> anions from the Al film with O<sup>2-</sup> and OH<sup>-</sup> cations from the electrolyte. The exchange of these ions results in two main reactions: 1) the growth of Al<sub>2</sub>O<sub>3</sub> at the Al/Al<sub>2</sub>O<sub>3</sub> interface and 2) the dissolution of Al<sub>2</sub>O<sub>3</sub> at the Al<sub>2</sub>O<sub>3</sub>/electrolyte interface [15]. These reactions cause the formation of alumina pores that proceed perpendicularly from the surface of the Al film. Upon reaching the embedded Fe layer, the anodization current rises by approximately 20 mA as the growth-front of the PAA breaks through the thin Fe layer and continues to grow into the bottom Al layer. In this way, the Fe catalyst becomes embedded in the Al<sub>2</sub>O<sub>3</sub> film, exposing it for catalytic activity at the inner pore sidewalls. Anodization is complete when the current falls below 1 mA, indicating complete oxidation of the Al and termination of the Al<sub>2</sub>O<sub>3</sub> formation at the Ti layer.

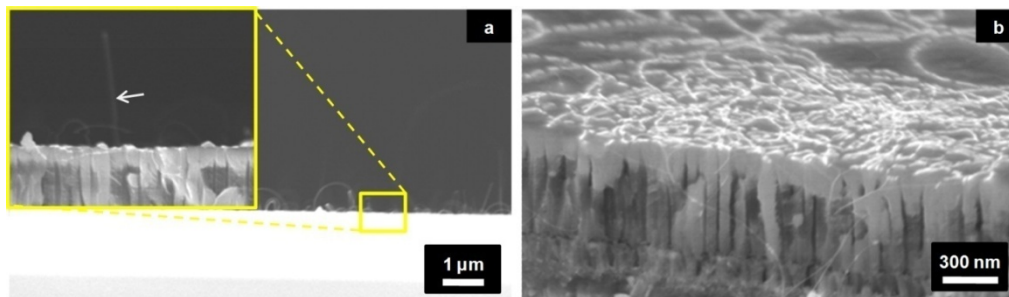


Fig. 2. Cross-sectional SEM images of (a) SWCNTs growing vertically from PAA and (b) SWCNTs draping along the PAA surface and appearing as bright strands.

Synthesis of the SWCNTs from the catalytically active PAA is accomplished in a hydrogen-fed MPCVD reactor with methane as the hydrocarbon precursor gas. Observations indicate that only one SWCNT nucleates in any given pore, likely because of the limited gaseous-carbon supply and the relatively high activation energy required for nucleation. After nucleating at the sidewall of a pore, the SWCNT proceeds to grow vertically to the surface of the PAA, toward the carbon supply. Evidence of this vertical growth is apparent in cross-sectional field-emission scanning electron microscope (SEM) images showing freestanding,

vertical SWCNTs, as shown in Fig. 2(a). However, most SWCNTs grow too long to remain vertical and instead lay horizontally across the PAA surface as seen in Fig. 2(b).

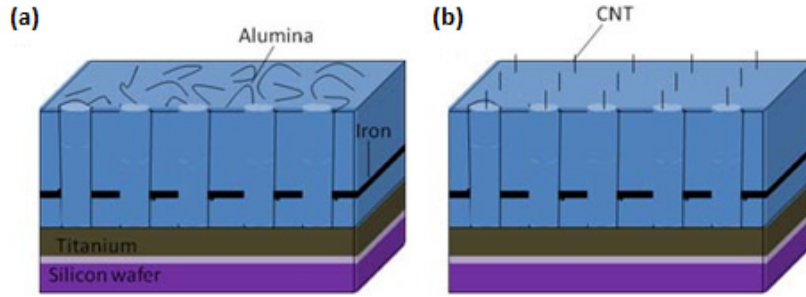


Fig. 3. (a) CNTs in PAA sample after ALD deposition of alumina; (b) CNTs in PAA sample after ALD deposition and final etches.

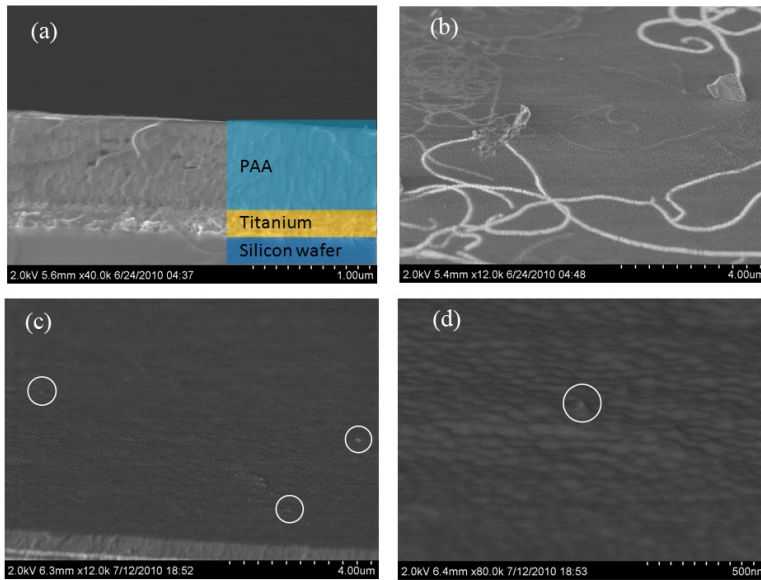


Fig. 4. (a) PAA sample with CNT growth and alumina coating from an ALD process, with a transparent color overlay on the right side to indicate the different parts of the metal stack. The iron layer was coated by the alumina. (b) Top view of PAA sample with CNT growth and alumina coating from an ALD process. (c) An RIE etch to expose CNT tips, and some examples of tips are circled. (d) Zoomed-in view of a CNT tip on the surface of the sample after anodization, CNT growth, ALD process of alumina, and final etches to obtain CNT tips. The tip is circled.

After CNT growth, the sample was coated with 30 nm of alumina by atomic layer deposition (ALD). The alumina conformally coats the sample; consequently the film is uniform in thickness and fills the pores while simultaneously coating the top surface. This results in an alumina sample 30 nm thicker than before with the pores filled. The CNTs remain on the surface, but they are coated with the alumina, as seen in Fig. 3(a). After the ALD process, the film is etched away using chromic acid for 6 minutes. Most of the CNTs are then etched away using an RIE process of 60 sccm of argon at 1 mtorr for 30 seconds at 300 W of coil power, leaving just tips sticking out of the sample. This results in an alumina sample of the same thickness as the previous PAA with CNTs sample, only with filled pores and CNT tips, to be used in measurements that call for vertical CNTs as in Fig. 3(b). A labeled microscope cross-sectional image of PAA with CNT growth and ALD coating is

shown in Fig. 4(a), with a top view of the same sample in Fig. 4(b). A top view of the sample after growth, ALD coating, and final RIE etch is shown in Fig. 4(c), with a magnified view of a CNT tip in Fig. 4(d).

As apparent in Fig. 4, the CNTs lying on the surface of the sample have disappeared. The RIE process etched away the overhanging CNTs, but the tips remain. However, the reduction to CNT tips has decreased the surface area covered by CNTs. The eventual ideal 1 to 1 CNT to pore growth can lead to better control of the optical properties.

### 3. Characterization of optical properties of ordered CNT arrays

#### 3.1 Hemispherical reflectance of CNT arrays grown in PAA

The hemispherical reflectance of the CNT array samples has been measured by a PerkinElmer Lambda 950 spectrometer with an integrating sphere. The experimental setup is shown in Fig. 5. The integrating sphere reflectance measurement allows for data to be taken over a wavelength range from 250 nm to 1100 nm.

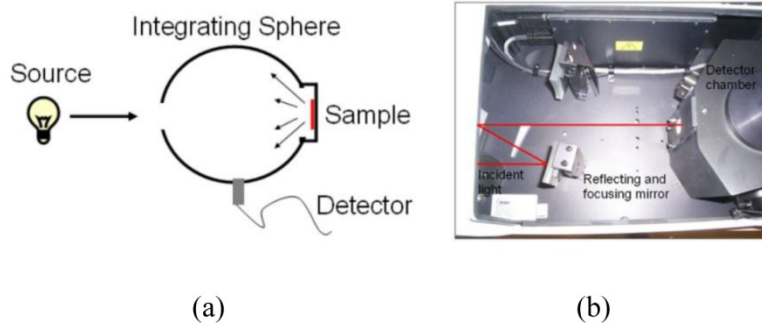


Fig. 5. (a) A sketch of integrating sphere measurement. (b) The actual experimental set-up.

The hemispherical reflectance for the PAA sample without CNT growth is shown in Fig. 6, along with the modeling results. Our model considers a three-layer system where a PAA layer with a thickness of  $d$  of 750 nm is sandwiched between a semi-infinite air layer and a semi-infinite titanium layer as the substrate. Each layer is assigned a complex refractive index  $m = n + i\kappa$ , where  $n$  is the refractive index, and  $\kappa$  is the extinction index, both of which depend on wavelength. For the PAA layer, the  $n$  and  $\kappa$  values for alumina, adopted from Ref [31], are used. To justify the semi-infinite assumption of the Ti layer, we calculate the penetration depth  $\delta_p$  using the following equation:

$$\delta_p = \lambda / 4\pi\kappa, \quad (1)$$

where  $\lambda$  is the wavelength. Using refractive index and extinction coefficient data of Ti in Ref [31], the penetration depth is found to range from 16.3 to 26.4 nm for an incidence wavelength range 247 – 1127 nm. Hence, the 100-nm Ti layer is much thicker than the penetration depth and can be assumed to be semi-infinite.

Light is incident from air with an angle  $\theta_1$  of  $8^\circ$ , which is the closest angle to the normal incidence that can be obtained practically with our spectrometer. Using the reflectance theory of multilayer thin films [32], the optical reflectance of the PAA layer can be calculated. The single-pass reflection coefficients on the air-PAA interface  $r_{12}$  and the PAA-titanium interface  $r_{23}$  are,

$$r_{12} = \frac{n_1 \cos \theta_1 - n_2 \cos \theta_2}{n_1 \cos \theta_1 + n_2 \cos \theta_2}, \quad r_{23} = \frac{n_2 \cos \theta_2 - n_3 \cos \theta_3}{n_2 \cos \theta_2 + n_3 \cos \theta_3}, \quad (2)$$

respectively. Here the subscripts 1, 2, and 3 represent air, PAA, and titanium respectively, and  $\theta_2$  and  $\theta_3$  are related to  $\theta_1$  by Snell's law,

$$n_1 \sin \theta_1 = n_2 \sin \theta_2 = n_3 \sin \theta_3. \quad (3)$$

The reflection coefficient, after summing up the contributions of multiple passes, is given by

$$r = \frac{r_{12} + r_{23}e^{-i2\delta}}{1 - r_{12}r_{23}e^{-i2\delta}}, \quad \text{where } \delta = \left(\frac{2\pi}{\lambda_0}\right) n_2 d \cos \theta_2. \quad (4)$$

Here  $\delta$  is the phase difference of the light created by traversing the PAA film twice, and  $\lambda_0$  is the incident wavelength in the air. The reflectance is finally calculated as

$$R = |r|^2. \quad (5)$$

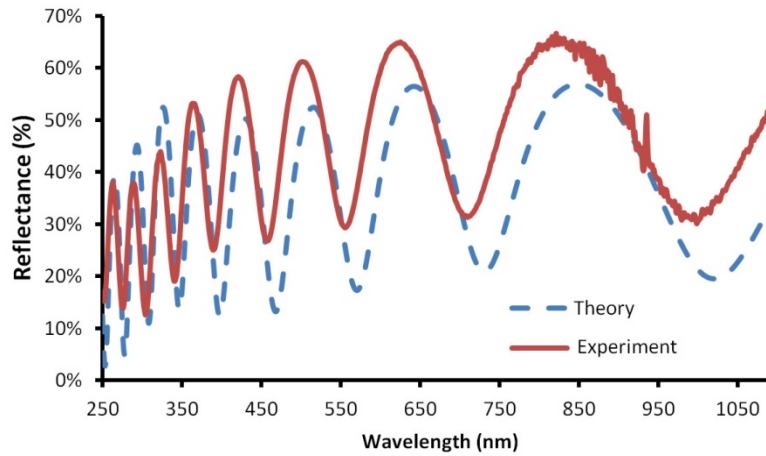


Fig. 6. A comparison between the theoretically calculated reflectance at 8 degrees and the measured reflectance for a 750 nm thick PAA sample.

The experimental and theoretical reflectance profiles show reasonably good agreement, with some discrepancy, as seen in Fig. 6. The oscillating profile manifests the interference of reflected EM fields from the first and second interfaces. This is commonly seen for thin films. The peaks and valleys of the two profiles are similar in periodicity, despite a systematic shift. The model overpredicts reflectance between 250 and 350 nm, and underpredicts it from 350 to 1100 nm. Several factors can be responsible for the discrepancy. First, there is probably uncertainty in our measurements of the PAA film thickness, so that the actual thickness may not exactly be 750 nm. Second, the anodized holes in actual samples are neglected in the theoretical calculations. Third, the interfaces in the actual samples are probably not ideally smooth, which can make the reflection partially specular and partially diffuse. This will be shown to be the actual case in the next section. The diffuse component will not show any interference effect. In addition, a small uncertainty may exist in the incident angle.

We also investigated how different steps in the PECVD process can affect the reflectance of the samples. Heating the sample to 900 °C, introducing the hydrogen plasma, and introducing the methane all change the reflectance properties of the PAA sample. As observed in Fig. 7, when the sample is heated to 900 °C, the reflectance of the sample decreases by 30-40%. Heating the sample to that temperature will cause the metal to expand, cracking and breaking the surface, drastically altering the surface structure and making it rougher, which can enhance light trapping and reduce reflectance. After plasma treatment, the hemispherical reflectance reduces another 5-10 percent, and the CNT growth reduces it

further by 2-3%. Adding in the plasma can break the nanopores on the surface, making it rougher. After CNT growth, CNTs add absorption to the light, thus reducing the reflection from the PAA/Ti interface. Overall, the reflectance is reduced more in the near-infrared (NIR) band than in the ultraviolet (UV) band, due to the fact that the samples are already more absorptive in the UV band.

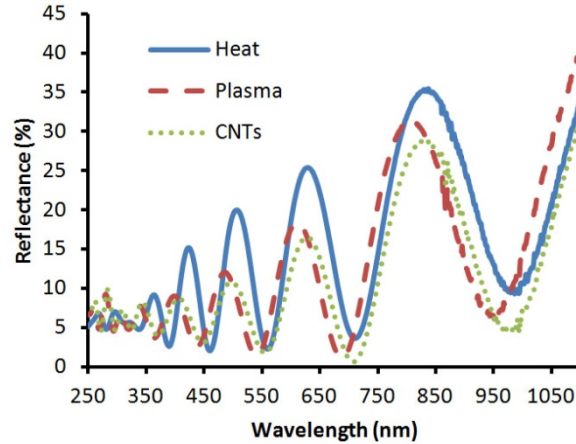


Fig. 7. Reflectance measurements at 8 degrees of the three pieces of PAA broken from the same original anodized piece and allowed to complete different steps of the CVD process: heating, plasma treatment, and CNT growth.

We also measured the hemispherical reflectance after each step in the full process: after the PAA construction, after CNT growth, after the atomic layer deposition (ALD) process, and after the final etch to expose the CNT tips. The results for reflectance are shown in Fig. 8. The reflectance profiles for PAA only and after CNT growth have been discussed earlier, and here we focus on the effects of ALD and final etching. The ALD process deposits 30 nm thick alumina to the top of the device, filling the pores and rendering a relatively smooth surface. Therefore, the reflectance increases and the peaks and valleys shift. After the chromic etch and RIE, however, the reflectance returns almost to the original profile with a slight increase. This is probably due to the exposure of the pores and CNTs.

### 3.2 Bi-directional reflectance distribution function

To reveal more specifics of the reflectance properties of the samples, we also performed bi-directional reflectance distribution function (BRDF) measurements. In BRDF

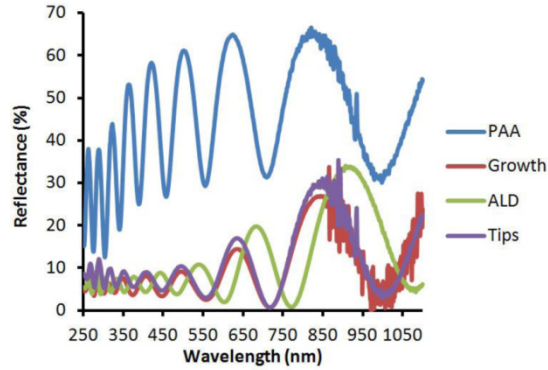


Fig. 8. A comparison of total reflectance at 8 degrees after each of the four steps in the full process. PAA: after PAA construction. Growth: after CNT growth. ALD: after the ALD process. Tips: after etching to expose the CNT tips.

measurements, the incident angle can be fixed, while the detection angle can vary continuously, allowing for measurements of both specular and diffuse components of scattering. This allows for more specific analysis of samples and angles. Distinct input angles can be chosen for the light, as can exact angles for the detected reflectance. However, if detection angle is set approximately equal to the input angle, specular reflectance dominates the peaks. Normalizing the data allows for more accurate measurements for the reflectance calculations. As shown in Fig. 9, all samples exhibit a large spike in the reflectance distribution function when the detection angle is the same as the incident angle, which indicates that specular scattering is strong. Also, as the incident angle increases, the magnitude of the reflectance peak increases, which is consistent with the trend for most materials. Interestingly, a second lobe exists at a slightly larger angle to the specular peak for all samples. The result with CNTs at  $35^\circ$  incidence is shown as a clear pattern. The surface roughness of the PAA sample is a major cause of typical observation of strong off-specular peaks due to masking and shadowing of the surface [33]. The roughness of the pre-anodized aluminum surface has been measured in prior work to be approximately 40 nm on the pre-anodized aluminum [34], and this value is expected to be representative of the porous alumina matrix. Torrance et al. [33] described an accurate model for the off-resonance peak in the reflectance from rough surfaces where the roughness is larger than the wavelength. This explanation was found to be valid also for certain sub-wavelength rough surfaces [35, 36].

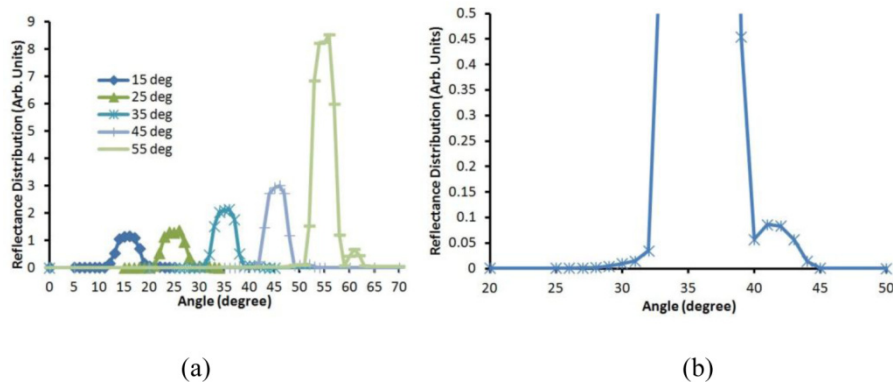


Fig. 9. (a) BRDF measurements of the sample with CNT tips poking out of an alumina substrate as a function of angle. The legend indicates the angle of incidence. (b) A magnified region of the BRDF at  $35^\circ$  incidence angle to highlight the secondary lobe.

#### **4. Conclusions**

In summary, we have synthesized ordered CNT arrays in PAA matrix under different processing conditions, and have characterized their total hemispherical optical reflectance and bi-directional reflectance distribution function (BRDF). For a PAA sample without CNT growth, the reflectance showed an oscillating pattern that can be explained by our model. Heating the PAA spectrally reduces the reflectance by 30-40%, and the plasma treatment reduces the reflectance by another 5-10%. After CNT growth, the reflectance further reduces by 2-3% since CNT has a high absorption of light. After the ALD process, the reflectance significantly increases due to the embedment of CNT arrays and nanopores. After etching and exposure of CNT tips, the reflectance almost returns to the original pattern with slightly higher reflectance. The bi-directional reflectance distribution function (BRDF) measurements indicate that our CNT-PAA surface is primarily specular, while the secondary lobe can be attributed to surface roughness.

#### **Acknowledgment**

This work was partially supported by the Air Force Office of Scientific Research through the Discovery Challenge Thrust (DCT) Program (Grants FA9550-08-1-0126 and FA9550-11-1-0057, Program Manager Joan Fuller). Fruitful discussions with Professor Zhuomin Zhang at the Georgia Institute of Technology and Dr. Hua Bao are gratefully appreciated.